TECHNISCHE MECHANIK
an open access journal

journal homepage: www.ovgu.de/techmech

Tech. Mech., Vol. 43, Is. 2, (2023), 211–219

Received: 03.04.2023
Accepted: 05.06.2023
Available online: 05.06.2023

A thermo-coupled constitutive model for semi-crystalline polymers at finite strains: Application across scales

Marie-Christine Reuvers[1]*, Sameer Kulkarni[2], Michael Johlitz[2], Alexander Lion[2], Tim Brepols[1], and Stefanie Reese[1]

[1] RWTH Aachen University, Institute of Applied Mechanics, Mies-van-der-Rohe-Str. 1, 52074 Aachen, Germany
[2] University of the Federal Armed Forces Munich, Institute of Mechanics, Werner-Heisenberg-Weg 39, 85577 Neubiberg, Germany

Abstract: Fiber reinforced thermoplastics are widely used for thermoforming and injection moulding processes, since their high strength to mass ratio is favorable for various industrial applications such as, for example, automotive engineering. Semi-crystalline polymers, as the composites matrix material, make up a subcategory of thermoplastics, which partly crystallize after cool-down from the molten state. They are reinforced with glass or carbon fibers to enhance their material performance. Nevertheless, during the thermoforming process, unwanted residual stresses can arise, due to the complex material behavior of semi-crystalline polymers under different temperatures and strain rates. The interaction between matrix and reinforcement being another unknown factor. Therefore, computational models are needed to predict the material response reliably and minimize production errors. This work presents a thermomechanically consistent phenomenological material formulation for thermoplastics at finite strains. In order to account for the highly nonlinear material behavior, elasto-plastic and visco-elastic contributions are combined in the model formulation. To account for the crystalline regions, a hyperelastic-plastic framework is chosen and extended with a tension-compression asymmetry in yielding. The material parameters, characterized using experimental results, depend on both, the temperature as well as the degree of crystallinity. Together with a linear elastic material model for glass fibers, the matrix formulation is embedded in a representative volume element with unidirectional fiber reinforcement to demonstrate the capabilities of the modeling framework in a multiscale context. A comparison of the virtual testing at varying temperatures and degrees of crystallinity to experimentally obtained results is planned as future work.

Keywords: Semi-crystalline polymers, Finite strains, Thermo-mechanical coupling, Model identification, Unit cell simulations

1 Introduction

In the class of polymers, thermoplastics, in contrast to thermosets or elastomers, can undergo reversible thermoplastic deformation due to their monomer arrangement on the microlevel, making them suitable for various industrial applications, such as forming processes or injection moulding. In addition, their high strength to weight ratio is attractive for use in cost-effective mass production of for instance car parts. Thermoplastics can be further subdivided into amorphous and semi-crystalline polymers (SCPs), where the latter show a complex visco-elastic, elasto-plastic material behavior in the finite strain regime due to their biphasic microstructure. During cool-down from the melt, the amorphous part slightly crystallizes, resulting in amorphous and crystalline phases. Hereby, the processing conditions, such as cooling rate, applied stress etc., influence the resulting degree of crystallinity (DOC) cf. Fornes and Paul (2003). The material behavior of SCPs is influenced not only by the deformation and temperature, various other factors such as loading rate (see e.g. Van Dommelen et al. (2003); Hao et al. (2022)), moisture content (cf. Sharma et al. (2020)), aging effects (cf. Rodriguez et al. (2020)) or the amount of crystalline phases (see e.g. Dusunceli and Colak (2008); Ayoub et al. (2011); Lion and Johlitz (2016); Felder et al. (2020a)) change the overall material response.
Resulting from the complex material behavior, the need for computational models arises, which can accurately predict the material response. Over the last decades, several constitutive frameworks were developed, based on the idea of Haward and Thackray (1968) and later Boyce et al. (1988) to decompose the total stress into contributions from molecular and intermolecular resistance. This approach has been used widely to model amorphous (e.g. Anand and Gurtin (2003); Barriere et al. (2019)) and semi-crystalline (e.g. Boyce et al. (2000); Felder et al. (2020b)) polymers rheologically. Several mechanical effects can be observed in SCPs, as for example a significant Bauschinger-like effect upon unloading Hasan and Boyce (1995) or pressure dependent yielding behavior Ghorbel (2008). Additionally, some works consider temperature effects e.g. Arruda et al. (1995); Anand et al. (2009); Johnsen et al. (2019) by introducing a coupling with the temperature field or investigating specific thermal effects, such as material self-heating for nylon (PA66) and polyamide 6 (PA6) at high loading rates (e.g. Maurel-Pantel et al. (2015); Hao et al. (2022)). The complex morphology of the underlying microstructures is taken into account by using modeling schemes that consider molecular dynamics Pisani et al. (2019) or the microstructural constituents using analytical homogenization Nikolov et al. (2002) or two-scale methods such as the FE^2 or FE-FFT-based method Gierden et al. (2022) to arrive at the macroscopic material response. Nevertheless, model identification of SCPs with experimental results remains challenging, since in most cases only limited comprehensive experimental studies exist, that take into account multiple influencing factors Felder et al. (2020a). Especially the DOC is difficult to test over a wide range, since specimen with a constant, temperature stable amount of crystallinity can't be obtained by relatively

* E-mail address: marie.reuvers@ifam.rwth-aachen.de
doi: 10.24352/UB.OVGU-2023-057

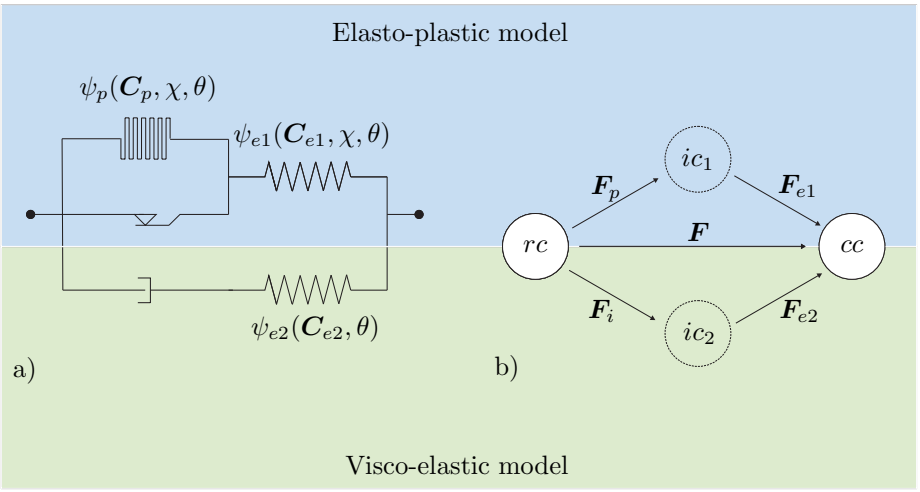

Fig. 1: a) Schematic illustration of the constitutive model b) Multiplicative splits of the deformation gradient

straightforward techniques, such as annealing. Here, more advanced approaches are necessary already during specimen production, as for example introducing a blending partner or crystallization agents.
In this work, a thermodynamically consistent material formulation for SCPs is developed (see Sec.2). Elasto-plastic and visco-elastic contributions are combined, to account for the highly nonlinear material behavior at large strains. In terms of influencing factors, both temperature and degree of crystallinity are considered. The resulting model framework is identified against experimental results (see Sec.3), conducted with an emphasis on the range of DOC for PA6. First computational results show good agreement with the experimental findings and the ability of the model to serve in structural simulations in the context of multiscale approaches (see Sec.4).

2 Constitutive modeling of semi-crystalline polymers

2.1 Kinematics

To describe the kinematic relations in a finite strain context, the deformation gradient $\boldsymbol{F}$ is introduced as well as the right Cauchy-Green tensor $\boldsymbol{C} = \boldsymbol{F}^T\boldsymbol{F}$ as the symmetric deformation measure in the reference configuration. In order to account for the influence of the biphasic microstructure on the macroscopic material behavior, a split of the deformation gradient into an elastic and a plastic part $\boldsymbol{F} = \boldsymbol{F}_{e1}\,\boldsymbol{F}_p$ (see e.g. Eckart (1948); Kröner (1959); Lee (1969)) is proposed corresponding to the materials' underlying intermolecular resistance. In terms of the molecular network, a split into elastic and viscous contribution $\boldsymbol{F} = \boldsymbol{F}_{e2}\,\boldsymbol{F}_v$ (see e.g. Sidoroff (1974); Lubliner (1985); Reese and Govindjee (1998)) is introduced (see Fig.1). According to the aformentioned split of $\boldsymbol{F}$ the corresponding intermediate configurations ic_1 and ic_2 are intoduced, alongside the elastic and plastic right Cauchy-Green tensors

$$\boldsymbol{C}_{e1} = \boldsymbol{F}_{e1}^T\boldsymbol{F}_{e1} = \boldsymbol{F}_p^{-T}\,\boldsymbol{C}\,\boldsymbol{F}_p^{-1}, \qquad \boldsymbol{C}_{e2} = \boldsymbol{F}_{e2}^T\boldsymbol{F}_{e2} = \boldsymbol{F}_v^{-T}\,\boldsymbol{C}\,\boldsymbol{F}_v^{-1}, \qquad \boldsymbol{C}_p = \boldsymbol{F}_p^T\boldsymbol{F}_p. \tag{1}$$

2.2 Constitutive relations

The total Helmholtz free energy is decomposed into an elasto-plastic ψ_1 and a visco-elastic ψ_2 energy based on the ideas of Haward and Thackray (1968); Boyce et al. (1988) regarding molecular network and intermolecular resistance. Additionally, a caloric energy contribution ψ_c related to the temperature-dependent specific heat is added

$$\psi = \psi_1 + \psi_2 + \psi_c. \tag{2}$$

In the above expression, the energy associated with elasto-plastic material behavior is the sum of an elastic contribution ψ_{e1} and a defect energy ψ_p associated with plastic deformations to account for the Bauschinger-effect observed in semi-crystalline polymers

$$\psi_1 = \psi_{e1}(\boldsymbol{C}_{e1}, \chi, \theta) + \psi_p(\boldsymbol{C}_p, \chi, \theta). \tag{3}$$

Both energies depend on the temperature θ as well as the degree of crystallinity χ, that is introduced as a constant input parameter for the formulation. The visco-elastic part on the other hand, consists of an elastic energy only

$$\psi_2 = \psi_{e2}(\boldsymbol{C}_{e2}, \theta). \tag{4}$$

Notworthy, in this part the dependence on the DOC is neglected, since the visco-elastic contribution is related to the amorphous parts of the microstructure. To ensure positive dissipation, the constitutive equations are derived in a thermodynamically consistent manner from the Clausius-Duhem inequality

$$\boldsymbol{S} : \frac{1}{2}\dot{\boldsymbol{C}} - \rho_0(\dot{\psi} + \eta\dot{\theta}) - \frac{1}{\theta}\,\boldsymbol{q}_0 \cdot \mathrm{Grad}(\theta) \geq 0, \tag{5}$$

defined with respect to the reference configuration, incorporating the second Piola-Kirchhoff stress tensor $\boldsymbol{S}$ and the density ρ_0. Taking the time derivative of the total Helmholtz free energy (2) and inserting it back into (5), yields

$$\boldsymbol{S} : \frac{1}{2}\dot{\boldsymbol{C}} - \rho_0\left(\frac{\partial\psi}{\partial\boldsymbol{C}_{e1}} : \dot{\boldsymbol{C}}_{e1} + \frac{\partial\psi}{\partial\boldsymbol{C}_{p}} : \dot{\boldsymbol{C}}_{p} + \frac{\partial\psi}{\partial\boldsymbol{C}_{e2}} : \dot{\boldsymbol{C}}_{e2}\right) - \rho_0\left(\frac{\partial\psi}{\partial\theta} + \eta\right)\dot{\theta} - \frac{1}{\theta}\boldsymbol{q}_0 \cdot \mathrm{Grad}(\theta) \geq 0. \tag{6}$$

Using the plastic and viscous velocity gradient $\boldsymbol{L}_* = \dot{\boldsymbol{F}}_*\boldsymbol{F}_*^{-1}, \quad * = p, v$, the equation can be reformulated and expressed in terms of the symmetric part of the velocity gradient, namely the rate of deformation $\boldsymbol{D}_* = \mathrm{sym}(\boldsymbol{L}_*)$. In addition, several stress quantities are introduced. Following the Coleman Noll procedure Coleman and Noll (1961), the total second Piola-Kirchhoff stress tensors is defined as $\boldsymbol{S} = \boldsymbol{S}_1 + \boldsymbol{S}_2$, containing the contributions from elasto-plastic $\boldsymbol{S}_1$ and visco-elastic $\boldsymbol{S}_2$ part

$$\boldsymbol{S}_1 = 2\rho_0\boldsymbol{F}_p^{-1}\frac{\partial\psi_{e1}}{\partial\boldsymbol{C}_{e1}}\boldsymbol{F}_p^{-T}, \quad \boldsymbol{S}_2 = 2\rho_0\boldsymbol{F}_v^{-1}\frac{\partial\psi_{e2}}{\partial\boldsymbol{C}_{e2}}\boldsymbol{F}_v^{-T}, \tag{7}$$

respectively. Similarly, the Mandel stress tensors $\boldsymbol{M}_1$ and $\boldsymbol{M}_2$ in the plastic and inelastic intermediate configuration, are defined as

$$\boldsymbol{M}_1 = 2\rho_0\boldsymbol{C}_{e1}\frac{\partial\psi_{e1}}{\partial\boldsymbol{C}_{e1}}, \quad \boldsymbol{M}_2 = 2\rho_0\boldsymbol{C}_{e2}\frac{\partial\psi_{e2}}{\partial\boldsymbol{C}_{e2}} \tag{8}$$

and the back stress $\boldsymbol{X}$ related to kinematic hardening follows to

$$\boldsymbol{X} = 2\rho_0\boldsymbol{F}_p\frac{\partial\psi_p}{\partial\boldsymbol{C}_p}\boldsymbol{F}_p^T. \tag{9}$$

To a priori fulfil the inequality, the entropy is stated as $\eta = -\partial\psi/\partial\theta$. The heat conduction is introduced following Fourier's law

$$\boldsymbol{q}_0 = -J\,\lambda_T\,\boldsymbol{C}^{-1}\,\mathrm{Grad}(\theta), \tag{10}$$

with $J = \det\boldsymbol{F}$ and $\lambda_T(\theta)$ denoting the temperature dependent heat conductivity. Inserting the aforementioned quantities back into Eq. (6) yields the reduced form of the Clausius-Duhem inequality

$$(\boldsymbol{M}_1 - \boldsymbol{X}) : \boldsymbol{D}_p + \boldsymbol{M}_2 : \boldsymbol{D}_v \geq 0. \tag{11}$$

In the following, the evolution equations for the plastic and viscous (rate of deformation $\boldsymbol{D}_p$ and $\boldsymbol{D}_v$ are derived to prove positive dissipation for the inelastic cases. According to Tschoegl (1971); Melro et al. (2013), a Tschoegl-type yield criterion

$$\Phi_p = 3J_2 + (m-1)\sigma_t I_1 - m\,\sigma_t^2 \leq 0 \tag{12}$$

is introduced, including the first $I_1 = \mathrm{tr}(\boldsymbol{M}_1 - \boldsymbol{X})$ and second $J_2 = 1/2\,\mathrm{tr}((\mathrm{dev}(\boldsymbol{M}_1 - \boldsymbol{X}))^2)$ invariant and thus accounting for the effects of hydrostatic pressure on the yielding behavior (see e.g. Ghorbel (2008)). Here, a tension-compression flow asymmetry is accounted for by introducing the ratio between compression σ_c and tension σ_t yield strengths

$$m = \frac{\sigma_c(\chi,\theta)}{\sigma_t(\chi,\theta)}. \tag{13}$$

Note here, that both yield strengths depend on the temperature as well as the degree of crystallinity. Under the assumption of associative plasticity, the plastic flow rule follows to

$$\boldsymbol{D}_p = \dot{\lambda}_p\frac{\partial\Phi_p}{\partial\boldsymbol{M}_1} = \dot{\lambda}_p\left(3\mathrm{dev}(\boldsymbol{M}_1 - \boldsymbol{X}) + (m-1)\,\sigma_t\,\boldsymbol{I}\right), \tag{14}$$

where $\dot{\lambda}_p$ denotes the plastic mutiplier. Finally, the Karush-Kuhn-Tucker conditions $\dot{\lambda}_p \geq 0$, $\Phi_p \leq 0$, $\dot{\lambda}_p\,\Phi_p = 0$ complete the elasto-plastic framework. Regarding the visco-elastic part, the evolution of the viscous deformation is chosen in line with Reese and Govindjee (1998) as

$$\boldsymbol{D}_i = \frac{1}{2\tau\mu_2}\mathrm{dev}(\boldsymbol{M}_2) + \frac{1}{9\tau K_2}\mathrm{tr}(\boldsymbol{M}_2)\boldsymbol{I}, \tag{15}$$

incorporating the bulk modulus $K_2(\theta)$ and the shear modulus $\mu_2(\theta)$. Here, the relaxation time $\tau(\boldsymbol{\tau}_2,\theta)$ is assumed to be a positive convex nonlinear function depending on the Kirchhoff stress in the current configuration $\boldsymbol{\tau}_2$ and the temperature. A specific function for the relaxation time is identified in Sec.3.2 with respect to experimental findings. As a next step, that is omitted here for brevity, the derived quantities are pulled back to the reference configuration to end up with two symmetric internal variables $\boldsymbol{C}_p$ and $\boldsymbol{C}_i$. For a detailed description of the pull-back operations, the reader is referred to Vladimirov et al. (2008); Brepols et al. (2020). To achieve a fully thermomechanically coupled framework, the energy balance must be exploited additionally, to derive the internal heat sources that allow modelling of for example self-heating phenomena. Since the scope of the paper lies predominantly on the model identification of the isothermal model, this step is omitted here.

Note on thermodynamic consistency

A more detailed derivation of the elasto-plastic model part, can be found in e.g. Vladimirov et al. (2008); Brepols et al. (2020). Here, the classical von-Mises yield criterion is exploited in a framework considering isotropic as well as kinematic hardening, to derive the plastic flow rule and prove the thermodynamic consistency. In the same manner, the thermodynamic consistency of the presented model equations can be demonstrated using Reese and Govindjee (1998) as well.

2.3 Specific choice of the Helmholtz free energies

Up to this point, the constitutive equations were derived in a quite general manner. In this way, the ability of the model to adapt to varying thermoplastics is preserved. To proceed with the model identification to experiments, performed on PA6, however a specific choice of energies is needed. For the elasto-plastic part, a combination of a compressible Neo-Hookean type energy

$$\psi_{e1} = \frac{\mu_1}{2}\left(\mathrm{tr}(\boldsymbol{C}_{e1}) - 3\right) - \mu_1 \ln\left(J_{e1}\right) + \frac{\Lambda_1}{4}\left(\det(\boldsymbol{C}_{e1}) - 1 - 2\ln(J_{e1})\right) - 3\,K_1\alpha_T(\theta-\theta_0)\ln(J_{e1}), \tag{16}$$

based on the two Lamé constants $\mu_1(\theta,\chi)$ and $\Lambda_1(\theta,\chi)$ and a nonlinear plastic defect energy of Arruda-Boyce type

$$\psi_p = \mu^* \sum_{i=1}^{5} \frac{c_i}{\lambda_m^{2i-1}}\left(I_{1p}^i - 3^i\right), \qquad c_i = \left\{\frac{1}{2}, \quad \frac{1}{20}, \quad \frac{11}{1050}, \quad \frac{19}{7000}, \quad \frac{519}{673760}\right\}, \tag{17}$$

is chosen. Here, $\lambda_m(\theta,\chi)$ and $\mu^*(\theta,\chi)$ are material specific parameters (see e.g. Kaliske and Rothert (1997)) and $I_{1p} = \mathrm{tr}(\boldsymbol{C}_p)$ is the first invariant of the plastic right Cauchy-Green tensor. In terms of the visco-elastic contribution, again a compressible Neo-Hookean energy is introduced

$$\psi_2 = \frac{\mu_2}{2}\left(\mathrm{tr}(\boldsymbol{C}_{e2}) - 3\right) - \mu_2 \ln(J_{e2}) + \frac{\Lambda_2}{4}\left(\det(\boldsymbol{C}_{e2}) - 1 - 2\ln(J_{e2})\right) - 3\,K_2\alpha_T(\theta-\theta_0)\ln(J_{e2}), \tag{18}$$

depending on the Lamé constants $\mu_2(\theta,\chi)$ and $\Lambda_2(\theta,\chi)$. Both elastic energetic contributions are extended with a term related to the volumetric elastic thermal expansion with the coefficient of thermal expansion $\alpha_T(\theta)$, the reference temperature θ_0 and the elasto-plastic and visco-elastic bulk moduli K_1 and K_2, respectively. The determinants of the elastic deformation gradients are given as $J_{e1} = \det(\boldsymbol{F}_{e1})$ and $J_{e2} = \det(\boldsymbol{F}_{e2})$.

3 Model identification and validation

3.1 Experimental data base for polyamide 6

All experimental results used in this work, were conducted at the Institute of Mechanics, University of the Federal Armed Forces, Munich. The samples (type 1BA, DIN EN ISO 527-2:2012) were injection moulded from PA6 type B granulate, kindly provided by Bond Laminates (Lanxess), at Polymer Service GmbH Merseburg (PSM). To achieve temperature stable samples with a broad range of DOCs, a blending technique was used, where the PA6 granulate was compounded with an amorphous co-polymer (cyclic olefin copolymer (COC)) in a step prior to injection moulding. Here, four different ratios of PA6:COC (100:0, 85:15, 70:30, 55:45) were produced. The amorphous co-polymer was chosen such, that the mechanical and thermal material properties are comparable to pure PA6. In this way, sprecimen with four different DOCs (0.29, 0.24, 0.18, 0.15), were obtained. The corresponding differential scanning caliometry (DSC) measurement was taken from the first heating run and measured with a *Q2000* machine from *TA instruments*. An additional measurement on pure COC showed a DOC lower than 1%, which proves that no additional crystallization happens in the specimen due to the addition of COC. The tensile and relaxation tests used for model identification, were obtained using a *Zwick/Roell Z020* machine with 2000 N and 500 N force sensors. Prior to testing, the specimen were stored in a dry chamber (*MP Dry Cabinet IV ST*) at 40° C, until the moisture content measured less then 0.1 %.

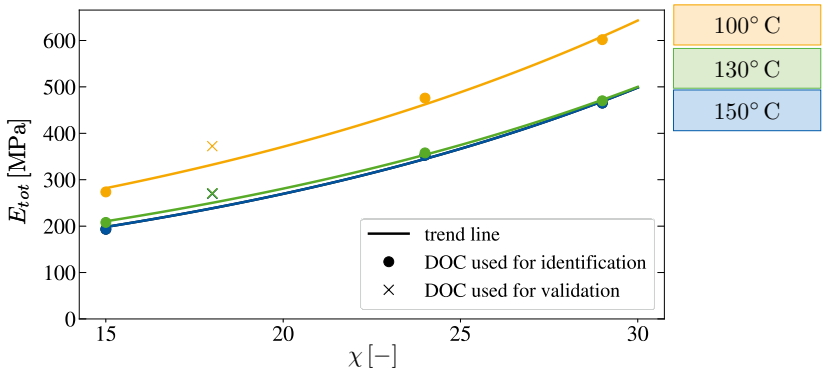

Fig. 2: Crystallinity dependence of the total Young's modulus above the glass transition temperature. The exponential trend line is of the form $E_{\mathrm{tot}}(\chi) = C_1 \exp(C_2\,\chi)$.

3.2 Parameter identification

In this section, a staggered parameter identification scheme is described, to achieve a unique set of parameters for each experimentally tested temperature, independent of the DOC. Note here, that the identification for the mechanical parameters is performed on the isothermal model. Throughout the identification procedure, only data from three DOCs (0.29, 0.24, 0.15) is used, leaving the data from $\chi = 0.18$ for validation purposes.

1. **Elastic quantities:** The elastic constants are obtained from the initial purely elastic material response, measured in monotonic tensile tests. Here, the total Young's modulus E_{tot} is taken according to DIN EN ISO 527-2:2012 and plotted against the DOC (see Fig. 2 a). Then, the Trust-Region algorithm is exploited, to obtain the dependence of the Young's modulus on the crystallinity. The identified exponential relation ($E_{\text{tot}}(\chi) = C_1 \exp(C_2\,\chi)$) is further implemented in the formulation. To determine the Poisson's, ratio several 2D digital image correlation (DIC) measurements were conducted, using the *LIMESS Q400 DIC* system. In this work, the Poisson's ratios of elasto-plastic and visco-elastic model part are assumed to be equivalent $\nu_{tot} = \nu_1 = \nu_2$.
2. **Viscous properties:** Following the identification of the elastic regime, the relaxation time τ is identified in a nonlinear manner, based on a post-processing scheme from Amin et al. (2006). To this end, the overstress $\boldsymbol{\sigma}_2$ under large deformations ($\varepsilon_{max} = 0.15$) is obtained from the long-term relaxation test data (see Felder et al. (2020b)) and further utilized to identify the inelastic strain as well as the relaxation time for each experimental time step with Eq. 15. Note here, that an exponential map was used for time discretization. The governed nonlinear relation between relaxation time and Kirchhoff overstress $\boldsymbol{\tau}_2$ (see Fig. 3b) showed no clear trend regarding the DOC. Therefore, the relaxation time is approximated by means of an exponential law Schmid et al. (1935)

$$\tau = \tau_0 \exp\left(-\delta\, ||\boldsymbol{\tau}_2||\right), \tag{19}$$

where $||\boldsymbol{\tau}_2|| = \sqrt{\boldsymbol{\tau}_2 : \boldsymbol{\tau}_2}$, depending only on τ_0 and the exponent δ, omitting the dependence on the DOC. The additional material parameters are obtained by simultaneously minimizing the summed square of the difference between the relaxation time data obtained from the post-processing procedure and the fitted model response. To this end, a Trust-Region algorithm is utilized and the three DOCs are identified simultaneously without additional weighting factors. Fig. 3 shows the verification for $\chi = 0.18$ as well.

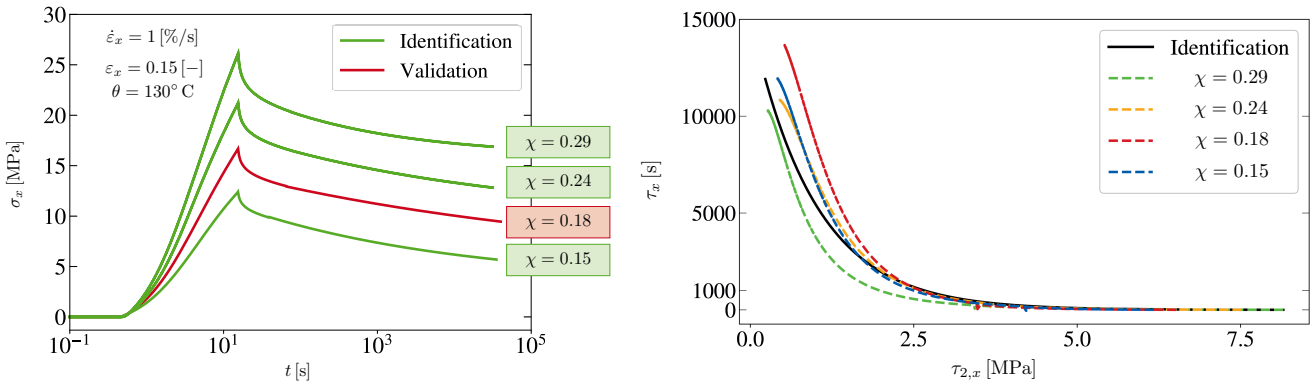

a) b)

Fig. 3: a) Longterm relaxation results at $\varepsilon_x = 0.15$ and 130°C b) Relaxation time overstress relation: Experimental data, characterization results (0.29, 0.24, 0.15) and validation (0.18) at 130°C.

3. **Plastic parameters:** In order to obtain the plastic material properties, the proposed framework is implemented into the commercial FEM software *ABAQUS* as a user material subroutine *UMAT*. The derivatives are generated via automatic differentiation utilizing the *Mathematica* plug-in *AceGen*. A monotonic, uniaxial tension test is performed on a single element, where the loading axis corresponds with the element's x-axis. Next, the obtained 3D stress-strain response is used, to simultaneously minimize the sum of the least-square residuals (defined as the difference between experimental and fitted Cauchy stress) for three degrees of crystallinity. For the identification, the Genetic algorithm in series with the Downhill-Simplex algorithm from the commercial software tool *MATLAB* are used, to determine the following material parameters: $\sigma_c, \mu^*, \lambda_m, E_1$. Note here, that the Young's modulus from the viscous part E_2 can be deduced from $E_2 = E_{\text{tot}} - E_1$. Due to the high test temperatures, the yield stress could not be identified directly from the experimental curves and is therefore treated as an additional identification parameter.

The results of the mechanical identification procedure are shown exemplary for 130° C in Fig. 4 and the corresponding parameter set in Tab. 1. In general, the results are well fitted to the experimental data, given the large span of DOC that is depicted by the model. Especially the prediction is in good agreement with the experimental findings. However it should be noted, that the onset of yielding could be improved in further calculations. The sudden change of stiffness at the yield onset, in combination with the high fitted ratio between E_1 and E_2 (see Tab. 1) suggests, that the elasto-plastic part needs

further flexibility in terms of the hardening law, which could be overcome by for example additionally introducing isotropic hardening.

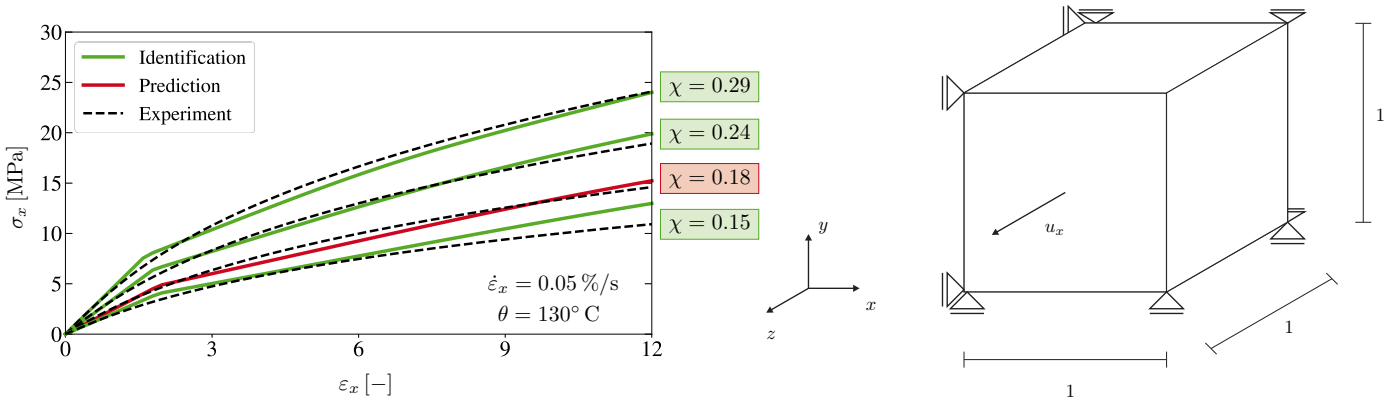

a) b)

Fig. 4: a) Monotonic, uniaxial tension - Experimental data and corresponding characterized (green) and predicted (red) model response at 130°C. b) Single element test - boundary value problem.

4. **Thermal quantities:** To distinguish the thermal conductivity of the PA6 compounds *Hot Disk* measurements are conducted at various temperatures. The resulting thermal conductivity λ_T is plotted over the DOC (see Fig. 5). In a second step the relation between λ_T and the DOC is estimated, using the Trust-Region algorith in *Matlab*. The results suggest a linear dependence of the DOC, which is incorporated in the model equations. In a similar manner, the crystallinity dependence of the other temperature related material parameters ρ_0 and α_T is identified, based on experimental findings (see Tab. 2).

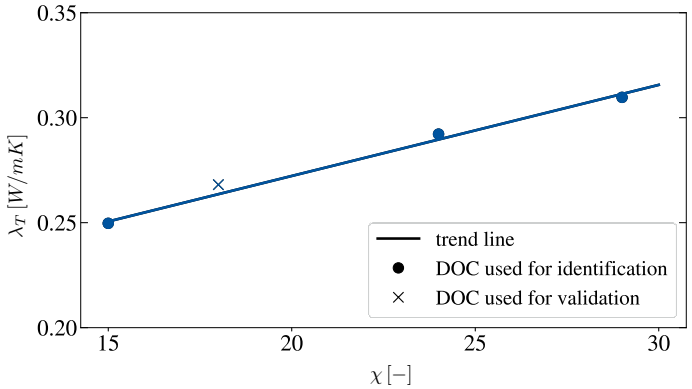

Fig. 5: Crystallinity dependence of the thermal conductivity. The linear trend line is of the form $\lambda_T(\chi) = C_1\,\chi + C_2$.

Tab. 1: Set of mechanical material parameters for 130 °C

$E_{\mathrm{tot}}(\chi) = C_1(\theta)\exp(C_2(\theta)\,\chi)$ $= (1 - m_E(\theta))E_2 + m_E(\theta)E_1$	$\nu_{\mathrm{tot}}(\theta) = \nu_1 = \nu_2$	$\sigma_c = \chi\sigma_c^0(\theta)$	$\sigma_t = \chi\sigma_t^0(\theta)$	$\mu^* = \chi\mu_0^*(\theta)$	$\lambda_m(\theta)$	$\tau = \tau_0(\theta)\exp(-\delta(\theta)\,\|\|\tau_2\|\|)$
$C_1 = 88.55$ [MPa] $C_2 = 5.771$ [-] $m_E = 0.847$ [-]	0.4 [-]	$\sigma_c^0 = 22.861$ [MPa]	$\sigma_t^0 = 22.861$ [MPa]	97.907 [MPa]	1.541 [-]	$\tau_0 = 15048.09$ [s] $\delta = 1.0183$ [-]

4 Numerical example: Glass fiber reinforced PA6

To demonstrate the models abilities in a structural example, a unit cell with unidirectional glassfiber reinforcement is chosen. The glass fiber distribution is randomized, using the random sequential adsorption (RSA) method (see e.g. Illian et al. (2008); Schneider et al. (2016)) to achieve a realistic fiber distribution from a production point of view. Here, a single ply is simulated, rather then a a laminate, therefore effects like for example delamination between plies are not considered. The interface bonding between fiber and matrix is chosen to be perfect in line with industry standards, where bonding agents are used frequently. A fiber volume fraction of 40% is assumed and the elastic fiber properties follow to $E_{\mathrm{fiber}} = 72$ [GPa] and $\nu_{\mathrm{fiber}} = 0.21$, the matrix properties are chosen according to Tab. 1. As in the model formulation elaborated above, the elastic fiber energy is chosen as of Neo-Hookean type. The unit cell geometry is generated in a periodic manner, as is the mesh, therefore periodic boundary conditions can be applied using so called equation constraints in *ABAQUS*. A schematic drawing of the unit cell and the two load cases is shown in Fig. 6. Two examples with different boundary conditions are conducted, in-plane tension and in-plane pure shear (see Fig. 6), for a

maximum strain of 10%. The contour plots show the Cauchy stress in x and xy direction at maximum strain. In the pictures, the stiffness contrast between fiber and matrix material is well represented. Additionally, pronounced compression regions are visible, especially for the pure shear case. In the regions, where fibers are being pushed closer together, localization phenomena are visible. Here, the use of finite element technology as for example using single Gauss point elements could help to overcome these problems. In order to verify the unit cell response, experimental tests on glass fiber reinforced PA6 at various temperatures are planned and will be compared to a statistically evaluated unit cell in terms of mesh and size convergence, similar to Melro et al. (2013).

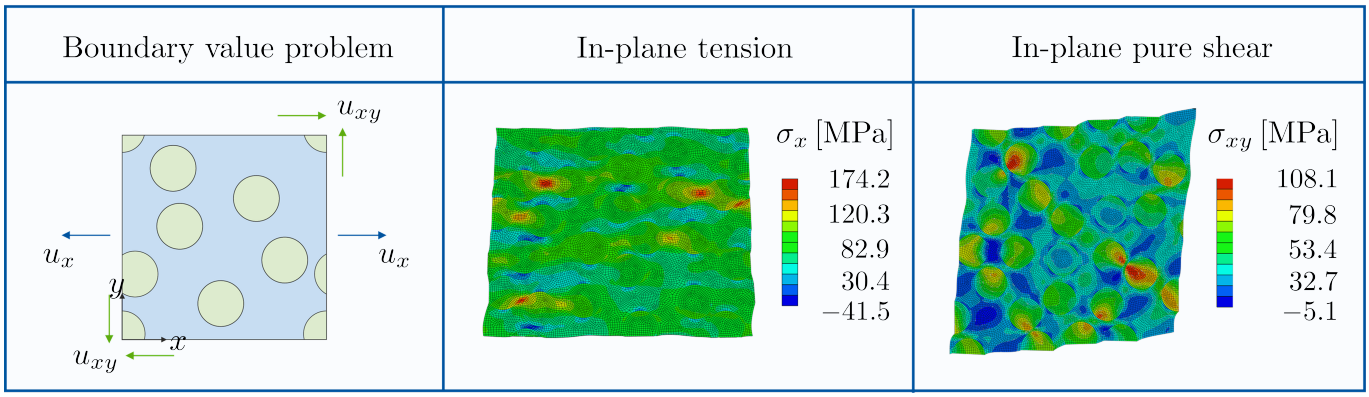

Fig. 6: a) Unit cell geometry with random fiber distribution and boundary value problems: in-plane tension (blue) and in-plan pure shear (green) b) Stress contour plots for in-plane tension and in-plane pure shear

5 Conclusion and outlook

In this work, a constitutive framework for the thermomechanical material behavior of semi-crystalline polymers is presented and characterized on the basis of an extensive experimental study on polyamide 6 at various temperatures. The proposed material model, consisting of a parallel arrangement of an elasto-plastic and viso-elastic part valid for finite strains, is developed in a thermodynamically consistent manner. Furthermore, the temperature and displacement field are fully coupled and the microstructure of PA6, represented via the degree of crystallinity is considered as an additional input parameter. The material parameters are governed using a staggered parameter identification scheme. Particular attention is paid on the determination of a unique parameter set per temperature, by simultaneously identifying multiple crystallinities. Compared to earlier works, the use of a blending technique during sample production, allowed testing on a wide range of crystallinities. In consequence, the model is characterized and validated for a crystallinity range of about 15%, here shown exemplary for 130° C, which to the authors knowledge has not been done yet. Due to a lack of a complete experimental database, further temperatures have not been validated until this point. However, the first results were in good agreement with experimental findings and showed the capability of the framework to predict the visco-hyperelastic elasto-plastic material response of PA6 at finite strains.
To fully characterize the material model in a mechanical and thermal sense, further experiments for other temperatures below and above the glass transition temperature are needed. After completion of the experimental data base, the remaining temperatures can be identified in a straightforward manner, using the proposed strategy. Here, the investigation of multiple strain rates is of particular interest. Furthermore, thermal and mechanical validation experiments for complex multidimensional stress states, as well as shear tests and infrared thermography measurements need to be conducted to validate the model further. Based on these results, the energetic contribututions can be revised, as for example proposed in Sec.3.2 to incorporate isotropic hardening or additional Maxwell elements if needed. The implementation in AceGen provides a flexible framework for that.
Regarding the use of the model formulation in a multiscale context, further experimental investigation is planned on a glass fiber reinforced PA6 single ply at various temperatures, as well as comparison to statistically generated unit cells. Hopefully these results lead to an insight of the material behavior on the mesoscale, that can be used to extend the presented formulation to an anisotropic macroscopic formulation in the future.

Tab. 2: Set of thermal material parameters for 130 °C

$\lambda_T = \chi\lambda_T^0$	$\alpha_T(\theta)$	$\rho_0(\theta)$	$c_p(\theta)$
$\lambda_T^0 = 1.32$ [W/mK]	$8.76 \cdot 10^{-5}$ [1/K]	$1.05 \cdot 10^3$ [g/mm^3]	2.2 [J/gK]

Acknowledgment and Funding Information

The author gratefully acknowledges the experimental data base conducted by Sameer Kulkarni at the Institute of Mechanics, University of the Federal Armed Forces, Munich. Financial support by the German Research Foundation (DFG) (RE 1057/52-1, project number 454873500) is gratefully acknowledged.

References

A.F.M.S. Amin, A. Lion, S. Sekita, and Y. Okui. Nonlinear dependence of viscosity in modeling the rate-dependent response of natural and high damping rubbers in compression and shear: Experimental identification and numerical verification. *International Journal of Plasticity*, 22(9):1610–1657, 2006.

L. Anand and M.E. Gurtin. A theory of amorphous solids undergoing large deformations, with application to polymeric glasses. *International Journal of Solids and structures*, 40(6):1465–1487, 2003.

L. Anand, N.M. Ames, V. Srivastava, and S.A. Chester. A thermo-mechanically coupled theory for large deformations of amorphous polymers. part i: Formulation. *International Journal of Plasticity*, 25(8):1474–1494, 2009.

E.M. Arruda, M.C. Boyce, and R. Jayachandran. Effects of strain rate, temperature and thermomechanical coupling on the finite strain deformation of glassy polymers. *Mechanics of Materials*, 19(2-3):193–212, 1995.

G. Ayoub, F. Zaïri, C. Fréderix, J.-M. Gloaguen, M. Naït-Abdelaziz, R. Seguela, and J.-M. Lefebvre. Effects of crystal content on the mechanical behaviour of polyethylene under finite strains: experiments and constitutive modelling. *International Journal of Plasticity*, 27(4):492–511, 2011.

T. Barriere, X. Gabrion, and S. Holopainen. A compact constitutive model to describe the viscoelastic-plastic behaviour of glassy polymers: Comparison with monotonic and cyclic experiments and state-of-the-art models. *International Journal of Plasticity*, 122:31–48, 2019.

M.C. Boyce, D.M. Parks, and A.S. Argon. Large inelastic deformation of glassy polymers. part i: rate dependent constitutive model. *Mechanics of materials*, 7(1):15–33, 1988.

M.C. Boyce, S. Socrate, and P.G. Llana. Constitutive model for the finite deformation stress–strain behavior of poly (ethylene terephthalate) above the glass transition. *Polymer*, 41(6):2183–2201, 2000.

T. Brepols, S. Wulfinghoff, and S. Reese. A gradient-extended two-surface damage-plasticity model for large deformations. *International Journal of Plasticity*, 129:102635, 2020.

B.D. Coleman and W. Noll. Foundations of linear viscoelasticity. *Reviews of modern physics*, 33(2):239, 1961.

N. Dusunceli and O.U. Colak. Modelling effects of degree of crystallinity on mechanical behavior of semicrystalline polymers. *International Journal of Plasticity*, 24(7):1224–1242, 2008.

C. Eckart. The thermodynamics of irreversible processes. iv. the theory of elasticity and anelasticity. *Physical Review*, 73(4):373, 1948.

S. Felder, H. Holthusen, S. Hesseler, F. Pohlkemper, T. Gries, J.-W. Simon, and S. Reese. Incorporating crystallinity distributions into a thermo-mechanically coupled constitutive model for semi-crystalline polymers. *International Journal of Plasticity*, 135: 102751, 2020a.

S. Felder, N.A. Vu, S. Reese, and J.-W. Simon. Modeling the effect of temperature and degree of crystallinity on the mechanical response of polyamide 6. *Mechanics of materials*, 148:103476, 2020b.

T.D. Fornes and Donald R. Paul. Crystallization behavior of nylon 6 nanocomposites. *Polymer*, 44(14):3945–3961, 2003.

E. Ghorbel. A viscoplastic constitutive model for polymeric materials. *International Journal of Plasticity*, 24(11):2032–2058, 2008.

C. Gierden, J. Kochmann, J. Waimann, B. Svendsen, and S. Reese. A review of fe-fft-based two-scale methods for computational modeling of microstructure evolution and macroscopic material behavior. *Archives of Computational Methods in Engineering*, 29(6):4115–4135, 2022.

P. Hao, V. Laheri, Z. Dai, and F.A. Gilabert. A rate-dependent constitutive model predicting the double yield phenomenon, self-heating and thermal softening in semi-crystalline polymers. *International Journal of Plasticity*, 153:103233, 2022.

O.A. Hasan and M.C. Boyce. A constitutive model for the nonlinear viscoelastic viscoplastic behavior of glassy polymers. *Polymer Engineering & Science*, 35(4):331–344, 1995.

R.N. Haward and G. Thackray. The use of a mathematical model to describe isothermal stress-strain curves in glassy thermoplastics. *Proceedings of the Royal Society of London. Series A. Mathematical and Physical Sciences*, 302(1471):453–472, 1968.

J. Illian, A. Penttinen, H. Stoyan, and D. Stoyan. *Statistical analysis and modelling of spatial point patterns*. John Wiley & Sons, 2008.

J. Johnsen, A.H. Clausen, F. Grytten, A. Benallal, and O.S. Hopperstad. A thermo-elasto-viscoplastic constitutive model for polymers. *Journal of the Mechanics and Physics of Solids*, 124:681–701, 2019.

M. Kaliske and H. Rothert. On the finite element implementation of rubber-like materials at finite strains. *Engineering Computations*, 1997.

E. Kröner. Allgemeine kontinuumstheorie der versetzungen und eigenspannungen. *Archive for Rational Mechanics and Analysis*, 4:273–334, 1959.

E.H. Lee. Elastic-plastic deformation at finite strains. 1969.

A. Lion and M. Johlitz. A thermodynamic approach to model the caloric properties of semicrystalline polymers. *Continuum Mechanics and Thermodynamics*, 28:799–819, 2016.

J. Lubliner. A model of rubber viscoelasticity. *Mechanics Research Communications*, 12(2):93–99, 1985.

A. Maurel-Pantel, E. Baquet, J. Bikard, J.-L. Bouvard, and N. Billon. A thermo-mechanical large deformation constitutive model for polymers based on material network description: Application to a semi-crystalline polyamide 66. *International Journal of Plasticity*, 67:102–126, 2015.

A.R. Melro, P.P. Camanho, F.M. Andrade Pires, and S.T. Pinho. Micromechanical analysis of polymer composites reinforced by unidirectional fibres: Part i–constitutive modelling. *International Journal of Solids and Structures*, 50(11-12):1897–1905, 2013.

S. Nikolov, I. Doghri, O. Pierard, L. Zealouk, and A. Goldberg. Multi-scale constitutive modeling of the small deformations of semi-crystalline polymers. *Journal of the Mechanics and Physics of Solids*, 50(11):2275–2302, 2002.

W.A. Pisani, M.S. Radue, S. Chinkanjanarot, B.A. Bednarcyk, E.J. Pineda, K. Waters, R. Pandey, J.A. King, and G.M. Odegard. Multiscale modeling of peek using reactive molecular dynamics modeling and micromechanics. *Polymer*, 163:96–105, 2019.

S. Reese and S. Govindjee. A theory of finite viscoelasticity and numerical aspects. *International Journal of Solids and Structures*, 35(26-27):3455–3482, 1998.

A. Rodriguez, B. Mansoor, G. Ayoub, X. Colin, and A. Benzerga. Effect of uv-aging on the mechanical and fracture behavior of low density polyethylene. *Polymer Degradation and Stability*, 180:109185, 2020.

E. Schmid, W. Boas, E. Schmid, and W. Boas. Kristallelastizität. *Kristallplastizität: Mit Besonderer Berücksichtigung der Metalle*, pages 15–24, 1935.

K. Schneider, B. Klusemann, and S. Bargmann. Automatic three-dimensional geometry and mesh generation of periodic representative volume elements for matrix-inclusion composites. *Advances in Engineering Software*, 99:177–188, 2016.

P. Sharma, A. Sambale, M. Stommel, M. Maisl, H.-G. Herrmann, and S. Diebels. Moisture transport in pa6 and its influence on the mechanical properties. *Continuum Mechanics and Thermodynamics*, 32:307–325, 2020.

F. Sidoroff. Un modèle viscoélastique non linéaire avec configuration intermédiaire. 1974.

N.W. Tschoegl. Failure surfaces in principal stress space. In *Journal of polymer science Part C: Polymer symposia*, volume 32, pages 239–267. Wiley Online Library, 1971.

J.A.W. Van Dommelen, D.M. Parks, M.C. Boyce, W.A.M. Brekelmans, and F.P.T. Baaijens. Micromechanical modeling of the elasto-viscoplastic behavior of semi-crystalline polymers. *Journal of the Mechanics and Physics of Solids*, 51(3):519–541, 2003.

I.N. Vladimirov, M.P. Pietryga, and S. Reese. On the modelling of non-linear kinematic hardening at finite strains with application to springback-comparison of time integration algorithms. *International Journal for Numerical Methods in Engineering*, 75(1): 1–28, 2008.